Earth and Space Science

RESEARCH ARTICLE
10.1029/2021EA002080

Imaging Considerations From a Geostationary Orbit Using the Short Wavelength Side of the Mid-Infrared Water Vapor Absorption Band

N. B. Miller[1,2], M. M. Gunshor[1,2], A. J. Merrelli[1,2], T. S. L'Ecuyer[1,3], T. J. Schmit[4], J. J. Gerth[5], and N. J. Gordillo[1,3]

[1]Cooperative Institute for Meteorological Satellite Studies, Madison, WI, USA, [2]Space Science and Engineering Center, Madison, WI, USA, [3]University of Wisconsin-Madison, Madison, WI, USA, [4]NOAA/NESDIS/Center for Satellite Applications and Research, Madison, WI, USA, [5]NOAA/NWS Office of Observations, Silver Spring, MD, USA

Key Points:

- Historically, the long wavelength side of the mid-infrared water vapor absorption band has been used for imaging
- Short wavelength (near 5 μm) spectral bands should be considered, especially with finer spatial resolutions
- Over most clear-sky surfaces, the reflective component ranges from small to zero for 5.1 and 5.6 μm bands

Correspondence to:
N. B. Miller,
nbmiller@wisc.edu

Citation:
Miller, N. B., Gunshor, M. M., Merrelli, A. J., L'Ecuyer, T. S., Schmit, T. J., Gerth, J. J., & Gordillo, N. J. (2022). Imaging considerations from a geostationary orbit using the short wavelength side of the mid-infrared water vapor absorption band. *Earth and Space Science*, *9*, e2021EA002080. https://doi.org/10.1029/2021EA002080

Received 13 OCT 2021
Accepted 31 DEC 2021

Author Contributions:
Conceptualization: A. J. Merrelli, T. S. L'Ecuyer, T. J. Schmit, J. J. Gerth
Data curation: N. B. Miller, M. M. Gunshor, A. J. Merrelli
Formal analysis: N. B. Miller, M. M. Gunshor, A. J. Merrelli, N. J. Gordillo
Funding acquisition: T. S. L'Ecuyer
Investigation: N. B. Miller, N. J. Gordillo
Methodology: N. B. Miller, M. M. Gunshor, A. J. Merrelli, T. S. L'Ecuyer, T. J. Schmit
Project Administration: T. S. L'Ecuyer
Resources: T. J. Schmit
Supervision: A. J. Merrelli, T. S. L'Ecuyer
Visualization: N. B. Miller, M. M. Gunshor, A. J. Merrelli

Abstract Historically, the long wavelength side (6–7.5 μm) of the mid-infrared water vapor absorption band has been used for imaging from the geostationary perspective. This began with the 6.4 μm band on Europe's Meteosat-1. While geostationary sounders for moisture profiling, including China's hyperspectral resolution infrared sounder and a planned sounder from Europe, are or will be measuring the short wavelength side of the water vapor band, this is not the case for geostationary imagers. Shorter wavelength (5–6 μm) spectral bands for imaging applications should be considered for observing moisture in the mid and lower troposphere because of several potential advantages offered by this spectral range. The short wavelength side of the water vapor band contains fewer additional absorbing gases that overlap the water vapor absorption lines. In addition, the shorter wavelengths would show less diffraction blurring which could enable finer spatial resolution for turbulence detection. This study considers some of the differences and potential advantages of the spectral information in the short wavelength side of the water vapor absorption band from the perspective of geostationary imaging. For dry conditions land heating could impact the qualitative use of observed brightness temperatures at 5.1 μm, while the solar reflection component over most clear-sky scenes is small for a 5.1 μm band and essentially zero for a 5.6 μm band.

Plain Language Summary Long before images are sent back to Earth from satellites, the needed spectral bands have to be specified. The band specification includes attributes such as the wavelength centers, widths, and signal-to-noise ratio. This paper investigates the rationale for including data from a region of the electromagnetic spectrum that has not been used for imaging from geostationary orbit. If implemented, these short wavelength water vapor bands would provide unique information regarding low-level moisture and mid-level turbulence. This paper quantifies the expected reflected component from the sun and the influence of land heating on observations, both of which are relatively larger at shorter wavelengths.

1. Introduction

Water, one of the most ubiquitous substances on Earth, naturally occurs in a triad of phases as either a solid, liquid or gas. The gaseous component of the water cycle is a key ingredient in regards to subsequent formation of precipitation, which ultimately provides necessary nourishment for the ecosystem. Measuring the occurrence and location of water vapor in the atmosphere is crucial for ensuring accurate weather forecasting, capturing energy transport, and investigating the radiative effects on atmospheric and surface conditions. Thus, it is important to observe the spatial distribution of water vapor at various altitudes.

The first geostationary orbit satellite with water vapor imaging capability was the Meteosat-1, a European Meteorological Geostationary Satellite launched in 1977. The Meteosat series carried an imaging radiometer with a 5.7–7.1 μm water vapor channel (Morel et al., 1978). Since that time, all the world's geostationary imagers have continued this tradition, although there have been additional spectral bands, with narrower spectral widths (Ackerman et al., 2019). The short wavelength side of the water vapor absorption band, approximately 5–6 μm, has fewer other absorbing gases, and should be considered for imaging applications. In fact, a number of designed, launched or to be launched, geostationary sounders employ the short wavelength side of the water vapor band, including the Geostationary Imaging Fourier Transform Spectrometer (Smith et al., 2009), the Geosynchronous Interferometric Infrared Sounder (GIIRS, Yang et al., 2017) and the hyperspectral Infrared Sounder (Holmlund

Writing – original draft: N. B. Miller, M. M. Gunshor, T. J. Schmit
Writing – review & editing: N. B. Miller, A. J. Merrelli, T. J. Schmit, J. J. Gerth

et al., 2021). For example, one of the spectral regions covered by China's GIIRS is 6.06–4.44 μm (1,650–2,250 cm^{-1}). There are many uses of geostationary sounders including information on temperature and moisture profiles, derived atmospheric stability, atmospheric composition (such as ozone), and the *u* and *v* components of the wind at various altitudes (Menzel et al., 2018; Schmit et al., 2009).

Even though the short wavelength side may be included by geostationary sounders, it also should be considered to add bands to the world's operational imagers at shorter wavelengths because imagers offer a faster refresh and finer spatial resolution. These bands may even be possible at a nominal 1 km resolution, allowing the resolution of finer features, such as atmospheric turbulence or moisture gradients. These new, short wavelength water vapor bands could supplement the current 16 spectral bands on advanced imagers, such as the Japan Advanced Himawari Imagers (Bessho et al., 2016), United States Advanced Baseline Imager (ABI, Schmit et al., 2017, 2018), Korea Advanced Meteorological Imagers (Choi & Ho, 2015) and Europe's Flexible Combined Imager (Holmlund et al., 2021). China's Advanced Geosynchronous Radiation Imager has 14 spectral bands, but subsequent versions will have 18 spectral bands (Yang et al., 2017). Currently the U.S. is defining its constellation and instrument suite for a geostationary suite as a follow-on to the GOES-R series.

As was done with the spectral selection of the GOES-16 Advanced Baseline Imager, there are many factors to consider (Schmit et al., 2005), including continuity with previous instruments and synergy with other instruments in low earth and geostationary orbits. Yet, advances are also needed to better monitor the earth-atmosphere system. A number of attributes may be competing, for example, a wider instrument response will improve the signal-to-noise ratio, but may also average over differing spectral features. Hence, when exploring new spectral bands, not only is the central wavelength an important consideration, but also the band's spectral width and shape. One of the main advantages of considering short wavelength bands for imaging purposes is that there is less blurring due to diffraction compared to longer wavelengths, allowing for finer spatial resolution. These enhanced images are desirable in order to detect water vapor features in greater detail and improve atmospheric turbulence detection.

This paper uses a spectral response function from the ABI to estimate the implications of shifting the central wavelength to the short wavelength side of the mid-infrared water vapor absorption band. Proposed bands are chosen to optimize remote sensing sensitivity of mid-level and low-level water vapor. A short wavelength water vapor band around 5.6 m would help better detect turbulence if spatial resolution is improved to nominally 1 km. A second band at 5.1 μm could sense lower level moisture, without interference from other absorbing gases. Weighting functions are modeled in order to determine the atmospheric pressure levels from which radiation is emitted. The weighting functions are compared to other existing ABI bands if applicable. A complete investigation also includes estimating the reflected solar component and diurnal surface temperature contribution to the observed brightness temperatures for a variety of environmental factors, including solar zenith angle, precipitable water vapor, and surface emissivity. These results will help inform decisions regarding the band selection of the next generation of geostationary imagers.

2. Imaging Bands in the Mid-Infrared Water Vapor Absorption Band

The radiative effects of atmospheric constituents, with the primary focus on water vapor, are simulated to understand how band selection will effect radiances and brightness temperatures (T_b). To test out a range of conditions we use six different standard atmospheres, including mid-latitude summer, mid-latitude winter, tropic, U.S. standard, sub-Arctic winter, and sub-Arctic summer profiles (McClatchey et al., 1972; Minzner, 1977). The standard profiles are input into a forward model to determine the resultant brightness temperatures and ultimately estimate the moisture detection capabilities.

Spectral signatures of seven gases of interest, as measured in the U.S. Standard Atmosphere (Figure 1, top panel), indicate the impacts (in T_b difference) caused by removing these atmospheric components individually using the fast radiative transfer model RTTOV v11.3 (Matricardi et al., 2001; Saunders et al., 1999), whereas the influence of 1000 DU of SO_2 was modeled with the Pressure–layer Fast Algorithm for Atmospheric Transmittances (Hannon et al., 1996). How radiation emitted from the Earth interacts with various absorbing gases, in clear-sky scenes, dictates where imager spectral bands are, or are not, placed. For example, if one wants to monitor SO_2 associated with volcanic eruptions, then one may want bands covering 7.3 and 8.6 μm. One also might want to utilize nearby spectral bands, such as 7.0 μm, that are not sensitive to SO_2 for baseline comparisons. In this paper

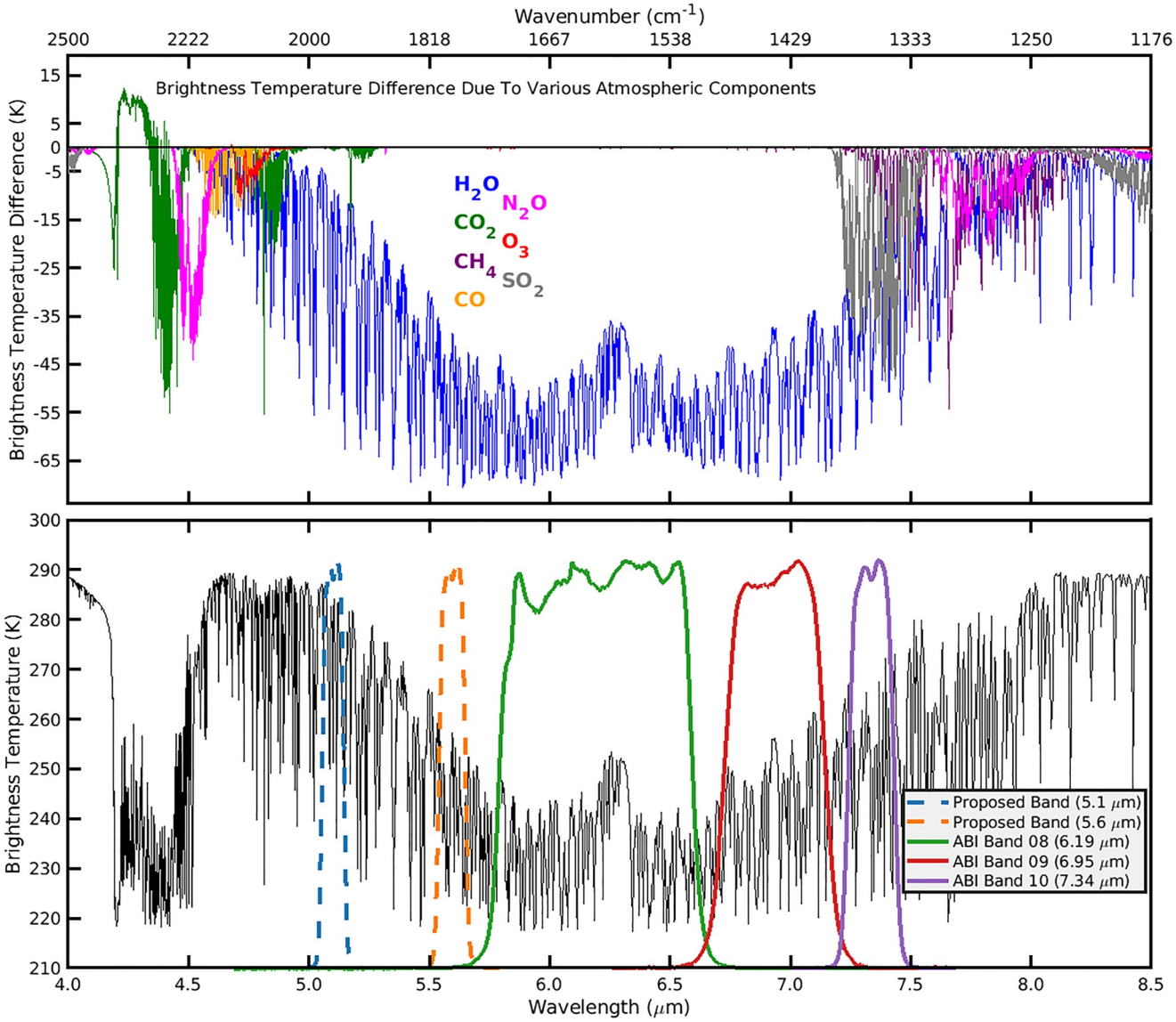

Figure 1. The top panel indicates the spectral impacts (in brightness temperature difference) of seven gases of interest (colored lines) as measured in the U.S. standard atmosphere spectrum, caused by removing these atmospheric components individually in a forward model. The bottom panel shows modeled brightness temperatures using the U.S. standard atmosphere. The spectral response functions of three GOES-16 Advanced Baseline Imager infrared bands and the two proposed bands we will explore in this paper are normalized and then scaled to illustrate overlap across the brightness temperature spectrum.

the focus is on improving the capability for monitoring H_2O, which has the wide and strong spectral signature from 5 to 8 μm (Figure 1, top panel).

2.1. Radiative Transfer Model

The radiative transfer model used to investigate two proposed bands at 5.1 and near 5.6 μm (to be introduced in Section 2.2) is the Principal Component-based Radiative Transfer Model (PCRTM, Liu et al., 2006). These exploratory center wavelengths are shorter than the ABI bands so it is necessary to model the solar contribution to simulated brightness temperatures using the PCRTM version 4.2 which is capable of modeling reflected solar radiation (Liu et al., 2016). The Infrared Atmospheric Sounding Interferometer (IASI, Hilton et al., 2012) instrument model within PCRTM is used to generate continuous radiance spectra covering the wavelength range 4.2–15.5 μm sampled at 0.25 cm^{-1}. The primary inputs to PCRTM are surface emissivity, solar zenith angle (SZA), skin temperature, surface pressure, profiles of atmospheric temperature, and concentration profiles of

Table 1
Total Spectrally Integrated Radiances Across ABI Bands 7–10 and the Two Proposed Bands Using the Spectral Radiances From a Modeled U.S. Standard Atmosphere

	Band width (cm^{-1})	Total radiance ($mW/(m^2\ sr)$)
ABI Band 7, 3.9 μm	125	231
Proposed Band 5.1 μm	35	436
Proposed Band 5.6 μm	35	246
ABI Band 8, 6.2 μm	210	2,107
ABI Band 9, 6.9 μm	87	2,486
ABI Band 10, 7.3 μm	35	1,925

Note. Each band width is calculated at the full-width-half-max of the spectral response function.

various atmospheric constituents across 101 pressure levels. The input profiles of temperature and various atmospheric molecules are from one of the six standard profiles mentioned above. The skin temperature is taken as the lowest level of the temperature profile and the surface pressure is set to 1,000 hPa. In Section 4 we investigate the effect on brightness temperature of changing targeted inputs including scaling the water vapor profile, varying the surface emissivity and SZA, and perturbing the skin temperature.

2.2. Proposed Bands

Satellite imagers measure across a range of wavelengths as described by spectral response functions (SRFs). A U.S. standard atmosphere is modeled to produce an example brightness temperature spectra from 2,500–1,176 cm^{-1} (4.0–8.5 μm), focusing on the water vapor absorption band centered at 6.3 μm (Figure 1, bottom panel). In addition, SRFs of three existing ABI bands and the two proposed imaging bands are overlayed across the brightness temperatures to give a sense of possible variations in observed T_b. Although the bottom panel of Figure 1 illustrates the range of brightness temperatures that fall within a given spectral response function (SRF), in practice the modeled spectral radiance must be convolved with a given SRF and then converted to T_b to get an accurate estimate of T_b for each band. The proposed bands shift (in wavenumber) the SRF of ABI Band 10 to a new center frequency. These proposed bands are an estimation using a relatively narrow SRF used on GOES-16 (ABI Band 10 centered at 7.3 μm is approximately 35 cm^{-1} wide at full-width-half-max). The simulations thus reflect what is possible from a theoretical standpoint, but in practice the actual spectral band characteristics are subject to specific instrument design and fabrication constraints that are not discussed in this work.

The peak of the blackbody emission occurs at longer wavelengths ($\lambda > 10$ μm) for typical earth surface and atmosphere temperatures, hence moving the SRF center to the short wavelength side of the water vapor absorption band generally implies a lower total spectrally integrated radiance. To estimate the effect, we compute the total spectrally integrated radiance using the peak normalized SRFs for the existing ABI bands as well as the proposed bands. These values are listed in Table 1. While the total radiance is much lower at the 5.6 μm center wavelength versus 6.9 μm, we note that the radiance is still comparable to the radiance for ABI channel 7 centered at 3.9 μm. The total integrated radiance at 5.1 μm is greater than of the band at 5.6 μm, although the magnitude is about 4–6 times smaller than ABI Bands 8, 9 and 10.

The spectrum in the bottom panel of Figure 1 shows that it should be possible to sense low level water vapor on either end of the water-vapor absorption band. However, examining top panel of Figure 1, there are multiple atmospheric gases at the long wavelength end, above 7.3 μm, that could interfere with sensing water vapor and only a weak and narrow band of CO_2 absorption (green line) near 5.2 μm that could interfere at the shortwave end. The impact of the absorbing gases N_2O and CH_4 on the longwave side of the water vapor absorption band are the same order of magnitude as H_2O. Scaling the water vapor profile of the U.S. standard atmosphere and then modeling the change in T_b using the SRF of ABI band 10 shifted to 7.9 μm results in a change in T_b of 0.035 K per 1% change in H_2O. The same sensitivity test for $N_2O(CH_4)$ results in a change in T_b of 0.041(0.030) K per 1% change in the $N_2O(CH_4)$ profile. The spatial and temporal variability of water vapor is generally greater than that of N_2O and CH_4, so to first order the measured T_b is related to the water vapor distribution. However, it is clear that changes in either N_2O or CH_4 could produce signatures in water vapor imagery that would be very difficult to characterize independently of the water vapor distribution if an imaging band was centered on the long wavelength side of the water vapor absorption band.

At the 5.1 proposed band the T_b sensitivity is 0.059 K per 1% change in H_2O, with no interfering gases. The proposed 5.1 μm band is narrow and it is possible that a real-world short wavelength band would need to be spectrally wider to get adequate signal-to-noise, in which case it may not be possible to completely avoid the CO_2 absorption at 5.2 μm. If the band did overlap the CO_2 absorption feature at 5.2 μm, the influence would be much less then that of water vapor. Modeling the brightness temperatures using the SRF of ABI band 10 shifted to 5.2 μm results in a T_b sensitivity of 0.074 K per 1% change in H_2O and only 0.006 K per 1% change in CO_2. Thus, one major

advantage of the short wavelength side of the water vapor band, where these proposed bands are located, is that it is relatively free from interference by other absorbing gases compared to the long wavelength side.

3. Simulating Band Characteristics

The first goal is to define a band on the short wavelength side of the water vapor absorption band to approximate the current ABI band at 6.9 μm. The second goal is to determine if a short wavelength band can be utilized for improved low level moisture detection. Since there is no target band for replication on the ABI or any other geostationary imager, we investigate the characteristics of a proposed band at 5.1 μm, as introduced in Section 2.2.

3.1. Spectral Convolution Method

To better understand the nature of the two proposed spectral bands, the first method convolves a shifted SRF curve with high spectral resolution data to see how the brightness temperatures vary. This convolution method is the same basic method used in satellite inter-calibration as employed by the Global Space-based Inter-Calibration System (Gunshor et al., 2009; Wu et al., 2009). By using polar-orbiting high spectral resolution IASI data, real earth scenes are used to simulate the proposed water vapor bands and allow comparison to the existing bands on the ABI. The ABI Band 10 (7.3 μm) SRF is spectrally adjusted to simulate the proposed bands, chosen because it is relatively narrow. The shape and width of the SRF in wavenumber space is maintained during the shift. The adjusted SRFs are convolved with both theoretical (U.S. Standard Atmosphere spectrum) and observed (IASI) spectra.

In the case of IASI, the data are convolved with the shifted spectral SRFs and are an accurate spectral simulation of the band on a geostationary sensor. The term "convolved" is widely used in this application, though it may be more accurate to describe the process mathematically as a weighted average:

$$CR = \frac{\int_{\nu_1}^{\nu_2} R(\nu)S(\nu)d\nu}{\int_{\nu_1}^{\nu_2} S(\nu)d\nu} \quad (1)$$

where CR is the Convolved Radiance, R is the IASI radiance at wavenumber ν, and S is the spectral response at wavenumber ν. In this method an average IASI radiance is calculated, weighted by the shifted SRF, for each IASI pixel, or Field of View (FOV). This is a useful method to simulate the spectral characteristics of these proposed bands, however the spatial resolution of IASI is not high enough to truly provide a sense of how images from a 1 km or even a 2 km imager band will look. This method does provide a quantitative method of comparing proposed bands to existing bands. Since most users prefer to look at brightness temperatures, a modified Planck function is employed to convert the radiances, identical to the method used operationally for the ABI (Schmit & Gunshor, 2020).

To get an initial estimate of where to center a band near 5.6 μm in order replicate the brightness temperature measured at 6.9 μm, the SRFs were convolved with a high spectral resolution (0.1 cm^{-1}) U.S. Standard Atmosphere radiance spectrum and the resulting radiance was converted to a brightness temperature. For the ABI 6.9 μm band, this calculation gives a brightness temperature of 244.231 K. A range of shifted central wavelengths are tested, starting at the SRF centered at 5.5 μm (1,818.18 cm^{-1}) and repeated for the SRF centered every cm^{-1} for ±40 cm^{-1} in order to find a close match to the 6.9 μm. Using this method, the closest match was centered at 5.595 μm with a brightness temperature of 244.237 K. The simulation with the U.S. Standard Atmosphere is a reasonable place to start, but the analysis is limited to the replication of brightness temperature. In Section 3.2, weighting functions are used to analyze the measurements vertically since replicating the 6.9 μm band can be more complicated on scenes with different temperature and moisture profiles.

An illustrative case study from a recent scene over the Pacific Ocean provides insight into how using existing and proposed bands capture non-uniform amounts of water vapor at various levels of the atmospheric column. A RGB true-color image from GOES-West (Figure 2) provides the context for two IASI granules that are investigated across the various spectral bands. The case occurs east of the Hawaiian Islands, on 07 December 2020 with a start time of 18:00:00 UTC, ~1.5 hr after sunrise. Two adjacent granules from IASI on METOP-A at 17:59:55 UTC, which are indicated by the cyan polygon in Figure 2, will be utilized in this section and in Figures 3–5. Concurrent

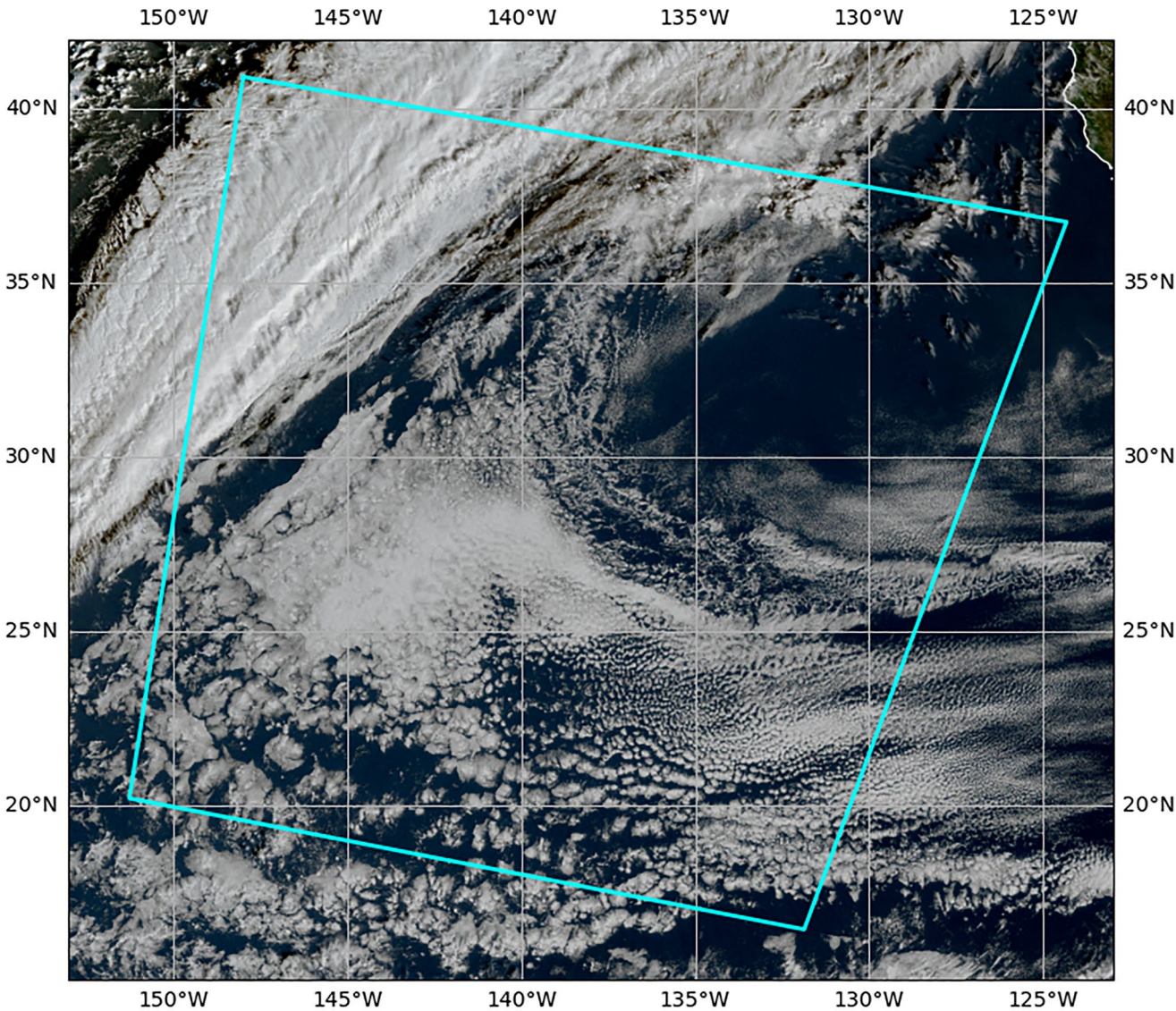

Figure 2. RGB true-color image from the advance baseline imager instrument on GOES-West, using the Full Disk scan starting at 2020-12-07 18:00:00. The cyan line shows the polygon associated with the two infrared atmospheric sounding interferometer granules shown in Figures 3, 4, and 5.

ABI products indicate a high altitude cloud band in the northwest section of the cyan bounded region, with a cloud top height of 10–12 km. In addition, there is a low level cloud deck in the center to west-center part of the image, with a cloud top height of 1–2 km. The scene contains a variety of cloud types and apparent clear-sky regions, ideal for investigating band characteristics.

Convolution with IASI granules provide qualitative and quantitative analysis of how well the proposed 5.6 μm band replicates the measurements from the 6.9 μm band. After convolving every FOV in the scene with both the simulated 5.595 μm and the ABI 6.9 μm SRFs and converting to brightness temperature, images were generated for comparison. Figure 3 shows that the 5.595 μm band (left panel) and the 6.9 μm band (middle panel) appear nearly identical, qualitatively. The right panel in Figure 3 quantifies the differences (5.595 band minus 6.9 μm band) that are not easily detectable by the human eye, resulting in a mean difference for this scene of 0.3°C and ranging from −0.4°C to 2.0°C. The northern middle region of the scene (lighter green in left and middle panels of Figure 3) yield the smallest absolute differences (closest to 0 K) in the right panel of Figure 3. The largest positive differences are in the areas of the high cloud deck (left upper region) and broken cloud field (middle upper region).

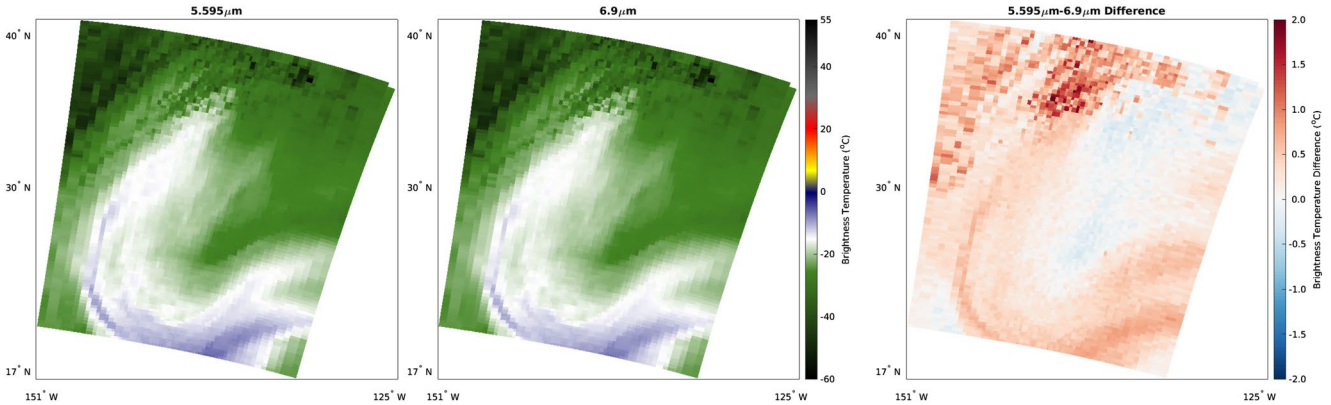

Figure 3. Images of the simulated 5.595 μm band (left), the simulated 6.9 μm band (advanced baseline imager band 09, middle), and the 5.595–6.9 μm difference (right). These infrared atmospheric sounding interferometer granules are from METOP-A on 07 December 2020 at 17:59:55 UTC and are coarser spatial resolutions than would be from an advanced geostationary imager. Region is indicated in Figure 2.

Convolution of the proposed 5.1 μm band with IASI is used to determine if a band on the short wavelength side of the water vapor band is able to sense low-level water vapor. Comparing the 5.1 μm band to an infrared window band (ABI band 14, 11.2 μm) indicates if the proposed band is sensing surface emission, while comparing the 5.1 μm band to the lowest level ABI water vapor band (ABI Band 10, 7.3 μm) shows sensitivity to unique water vapor features at a level not currently being sensed by the ABI. The left panel in Figure 4 shows what the 5.1 μm band would look like for the same scene shown in Figure 3. Note that the brightness temperature scale is the same as in left and middle panels of Figure 3. This band sees some similar water vapor features as the 6.9 or 5.595 μm bands, but the warmer brightness temperatures suggest a detection of water vapor deeper into the atmosphere, closer to the surface. In contrast, the 11.2 μm ABI band is a fairly clean window band with only small water vapor absorption, but mostly receiving signal from the surface or the tops of clouds (middle panel of Figure 4). The cooler low level clouds are indicated by the orangish-yellows in the 11.2 μm image (middle panel) and correspond to cooler temperatures in the 5.1 μm image (left panel), thus limiting the ability to detect low level water vapor in these regions. The right panel in Figure 4 shows that the 7.3 μm ABI band would sense much cooler brightness temperatures than the 5.1 μm band.

The prominent water vapor feature of this scene is evident in the warmer brightness temperatures of the 5.1, 5.6, 6.9, and 7.3 μm band images (Figures 3 and 4). This water vapor feature could be described as a lower-case letter "u", somewhat skewed to the east and is not evident in the 11.2 μm band (Figure 4). In what might be considered the cradle of the "u" shape and also at the upper left interior section of this water vapor feature there are differences between the 6.9 and 5.1 μm bands. In Figure 3 the 6.9 μm, or 5.595 μm band, is generally colder (white

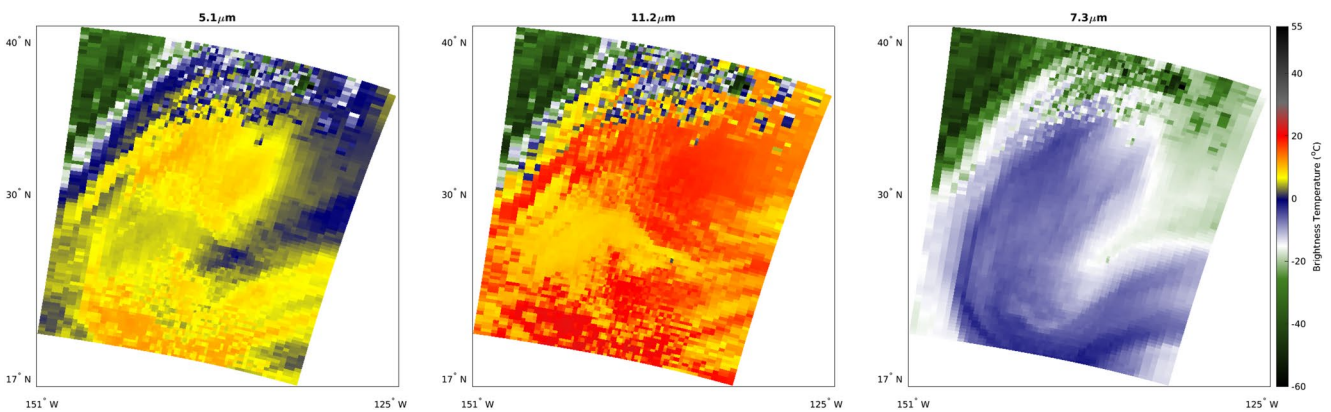

Figure 4. Images of the simulated 5.1 μm band (left), the simulated 11.2 μm band (advanced baseline imager (ABI) band 14, middle) and the simulated 7.3 μm band (ABI Band 10, right). These IASI granules are from METOP-A on 07 Dec 2020 at 17:59:55 UTC and are coarser spatial resolutions than would be from an advanced geostationary imager. Region is indicated in Figure 2.

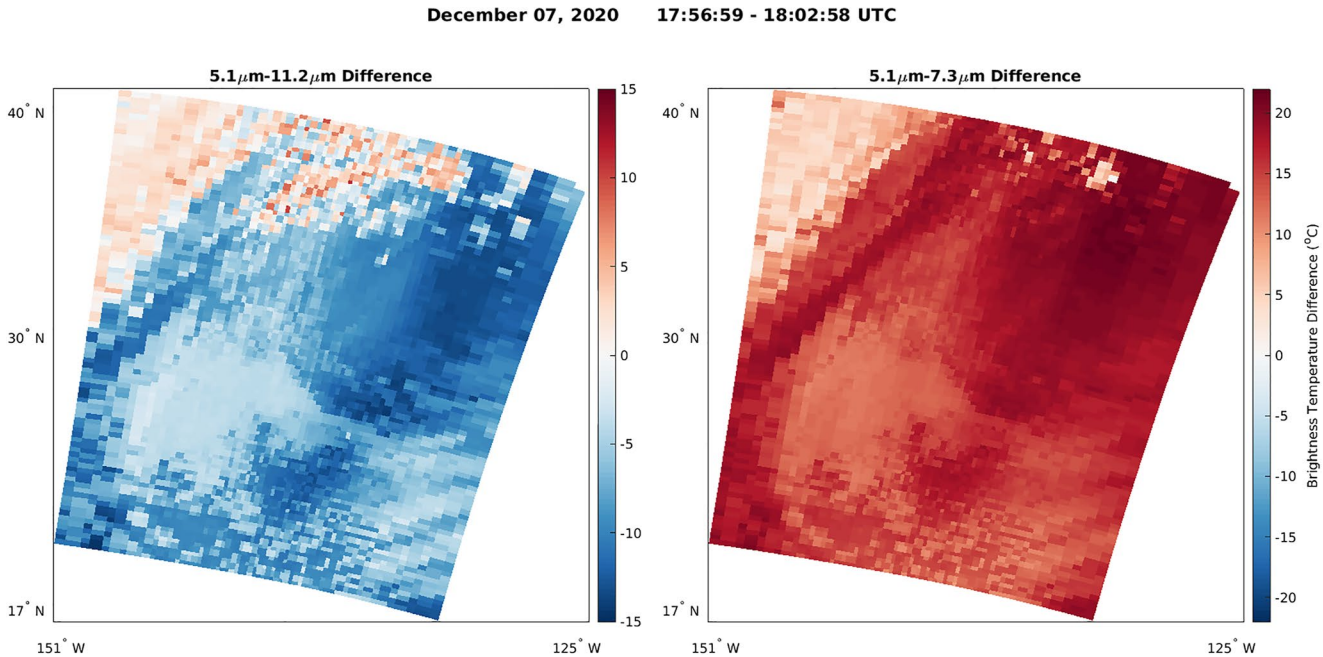

Figure 5. Differences of the images in Figure 4. The left panel is the simulated 5.1 μm band minus the simulated 11.2 μm band advanced baseline imager (ABI band 14). The right panel is the simulated 5.1 μm band minus the simulated 7.3 μm band (ABI Band 10). Region is indicated in Figure 2.

or light green) in these aforementioned areas compared to the bottom of the "u"-shape (purple). The contrast between the bottom of the "u"-shape and both the cradle and upper left interior section of the water vapor feature is less pronounced in the 5.1 and 7.3 μm band images (Figure 4) indicating a more uniform distribution of water vapor at lower levels in the atmosphere. In general, the 5.1 μm band image shows detailed brightness temperature variations due to the prominent water vapor feature and warmer brightness temperatures compared the other water vapor sensitive bands, indicating that the 5.1 μm band is useful for looking at unique aspects of low level water vapor features.

To further investigate the differences between the bands in Figure 4, Figure 5 shows the 5.1 minus 11.2 μm band difference (left panel) and the 5.1 minus 7.3 μm band difference (right panel). Generally, presence of high and low clouds reduces the differences between bands. One exception is the high clouds in the northwest region, where the brightness temperatures are warmer in the 5.1 μm band. The higher brightness temperatures could be due to changes in the spectral emissivity of the ice clouds between the two wavelengths, or due to solar reflection at the shorter wavelength that is not present at 11.2 μm. Increases in brightness temperatures due to surface reflection of solar radiation will be considered in Section 4.1, but solar reflection off of clouds are not a main concern because it is difficult to observe low level water vapor below a cloud deck regardless if it is day or night. The aforementioned cradle and the upper left interior section of the "u"-shape are where the biggest differences in the water vapor feature appears as deeper blues (left panel) and deeper reds (right panel). In these areas the 5.1 μm has much colder brightness temperatures compared to the surface (deeper blue) and much warmer brightness temperatures compared to 7.3 band (deeper red), both due to the presence of low level water vapor. Thus, the 5.1 μm band is well suited to provide insight into lower-level water vapor that none of the existing ABI bands can provide.

3.2. Weighting Function Method

The second method utilized in understanding the proposed bands was to generate weighting (or contribution) functions (WF) to visualize the relative contribution of atmospheric pressure layers to the emitted radiance. PCRTM is used to compute layer transmittance, on the standard 101 level grid, at the IASI instrument resolution (0.25 cm^{-1} sampling), covering the entire mid infrared (IR) range. The transmission from the top of the atmosphere (TOA) was then calculated using the PCRTM layer transmission for the wavelength range containing the ABI band. The ABI SRF was interpolated to the PCRTM wavenumber grid and the band transmission for each

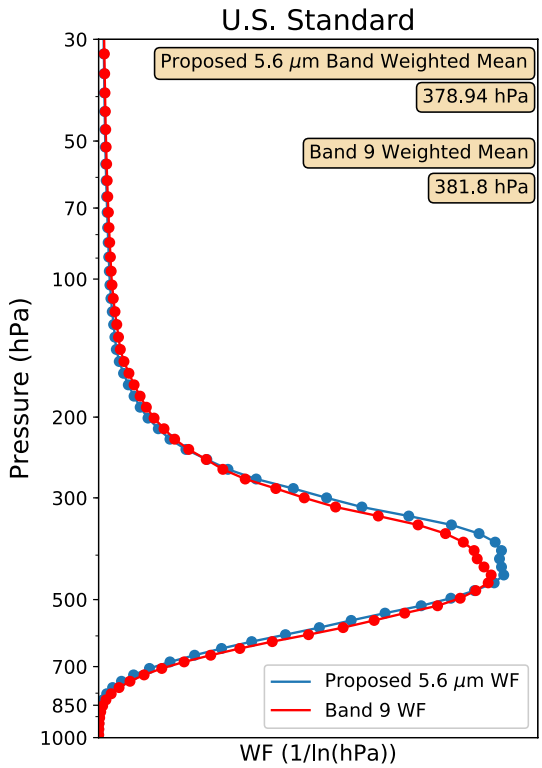

Figure 6. Weighting functions (WF) using the spectral response functions (SRF) from advanced baseline imager (ABI) Band 10 shifted to 5.6 μm (blue) and the SRF of ABI band 9 at 6.95 μm (red). Both weighting functions use the U.S. standard atmosphere as input into PCRTM.

layer was calculated by convolving the interpolated SRF with the TOA transmission. The WF was then generated by calculating dT/dln(P), where P is pressure and T is layer transmission. More on the concept of WF can be found at: https://cimss.ssec.wisc.edu/goes/wf/.

Weighted mean pressures of the WF on the short wavelength side of the water vapor absorption band are calculated in order to approximately match that of the 6.9 μm band. The weighted mean pressure of the WF takes into account the contributions from each layer as opposed to comparing the pressure level of the peak value of the WF which is dependent on model vertical resolution and independent of WF shape away from the peak. Using Band 9 SRF (Figure 1, bottom panel) to find the WF of the U.S. Standard atmosphere the weighted mean pressure is found to be 381.8 hPa. This weighted mean pressure is about 2.9 hPa more than that of the U.S. standard atmosphere calculated at 5.6 μm using Band 10 SRF. The aforementioned WFs are shown in Figure 6 and it is evident that the shapes are very similar, indicating that water vapor detection would be consistent at these two bands. The shape of the peak of the 5.6 μm WF is a bit flatter and is shifted upwards for most pressure levels, contributing to the weighted mean being at a higher altitude (lower pressure level).

As an independent check on the results from Section 3.1, which compares brightness temperatures to find the optimal wavenumber shift to match Band 9, a similar concept of comparing weighting functions is used to find an optimal shift. The weighted mean difference is calculated for each of the six standard atmospheres by shifting the Band 10 SRF in 0.001 μm increments. The small increments are for exploratory purposes since the ability to engineer the central wavelength to be this precise is not feasible. The results, depicted in Figure 7, are in agreement with Section 3.1 which found the optimal shift to be 5.595 μm using the U.S. Standard atmosphere. In fact, all six cases, which have different water vapor content and distributions, cross the zero difference marker between 5.595 and 6.0 μm. Interestingly, the weighted mean difference does not strictly decrease with an increase in the shifted wavelength value. This is because the shape of brightness temperature spectrum has a complicated structure and does not decrease monotonically with an increase in wavelength (Figure 1, bottom panel).

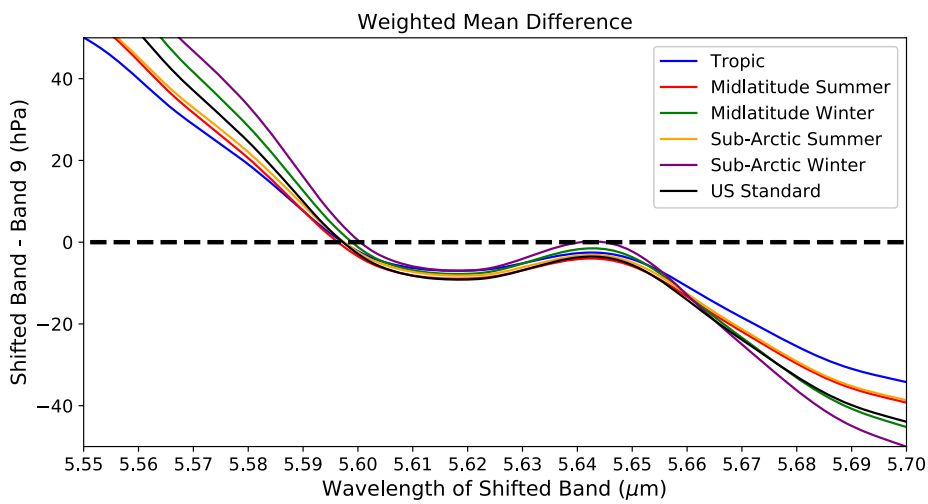

Figure 7. The weighted mean differences of the weighting functions using the six standard atmospheres listed in the legend. Weighted mean differences are calculated by subtracting the static weighted mean of advanced baseline imager Band 10 from the weighted mean at the shifted spectral response function at the given wavelength.

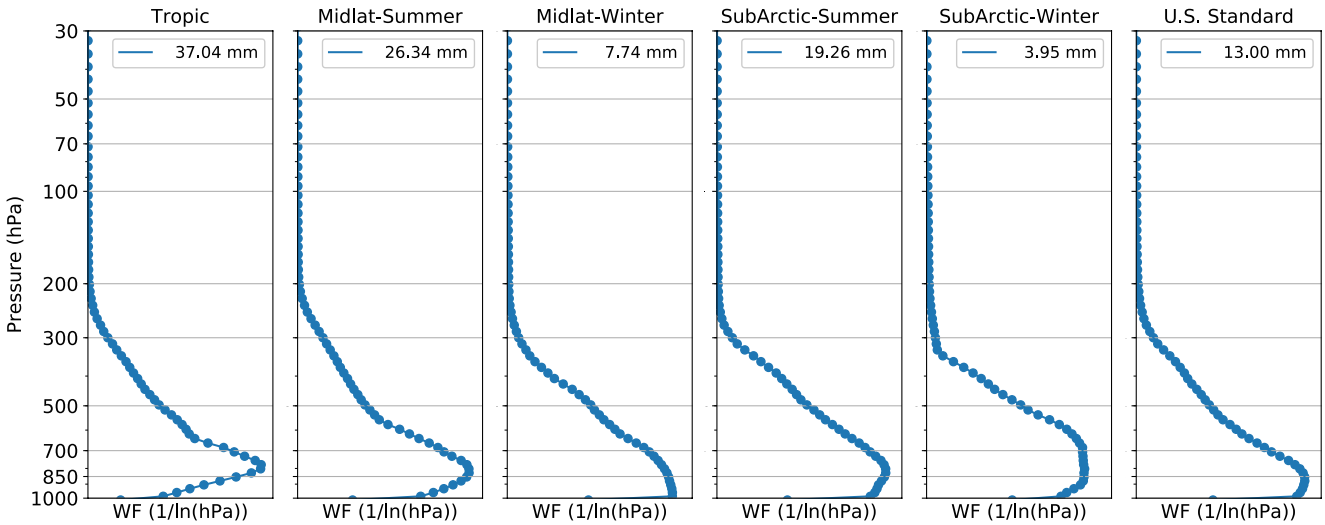

Figure 8. Weightings function for the proposed 5.1 μm band derived from one of the six standard atmospheres as indicated in the title. This spectral band is sensitive to the lower troposphere, peaking at higher pressure levels in dryer atmospheres and including more surface contribution. The precipitable water vapor (mm) is given at the top of each panel.

The weighting function technique is also used to investigate the proposed 5.1 μm band, sensitive to moisture in the lower troposphere. PCRTM is run for the six standard atmospheres at a solar zenith angle of zero. The precipitable water vapor (PWV) for each of these atmospheres differs according to the integrated amount of water vapor in the entire column. The PWV values and weighting functions for each case are shown in Figure 8. Cases with more moisture content result in a more elevated peak in the WF compared to drier atmospheres. It is evident that the 5.1 μm band would be useful in detecting moisture originating from pressure levels close to the surface. In winter these drier cases have their peaks at or close to the surface, indicating that the surface will be visible at 5.1 μm since a lack of moisture means the atmosphere will have increased transparency. Implications of surface contributions will be explored in Section 4.

4. Surface Considerations

As established in Section 2, water vapor is the primary absorbing gas for the proposed 5.1 and 5.6 μm bands. The lack of other absorbing gases is ideal for water vapor detection, although for a dry atmospheric columns it makes it more likely that the satellite sensor will detect radiation emitted by the surface or reflected from the Sun. The sources of radiation not originating from the atmosphere can be accounted for by using complimentary window bands which are not as sensitive to the amount of water vapor in the atmosphere. For completeness, we quantify the possible effects of solar radiation and surface emission on brightness temperature under a variety of conditions.

4.1. Solar Reflection

Solar radiation decreases sharply at wavelengths greater than 4 μm and this threshold is often used as a cut-off between shortwave and longwave radiation regimes (i.e., Driemel et al., 2018). Yet the magnitude of the TOA radiance at wavelengths greater than 4 μm that originates from the sun are substantial (Coddington et al., 2016). The incident radiance at the TOA passes through the atmosphere with a path length determined by the SZA. Next, solar radiation is reflected by the surface before making a return trip through the atmosphere to the satellite as determined by the sensor zenith angle. For Lambertian reflection the reflectively is the amount of radiation that is not absorbed at a given wavelength, thus, reflectivity is estimated as 1.0 minus the surface emissivity (ϵ). Figure 9 shows the emissivity across the Continental United States (CONUS) at 5.1 and 5.6 μm on 1 June 2020. The emissivity at these specific wavelengths was derived using hingepoints from the UW-Madison baseline fit (BF) global emissivity data (Seemann et al., 2008) to obtain high spectral resolution values via the UW High Spectral Resolution Emissivity Algorithm (Borbas & Ruston, 2010). In general, the reflectivity at 5.6 μm is less than that

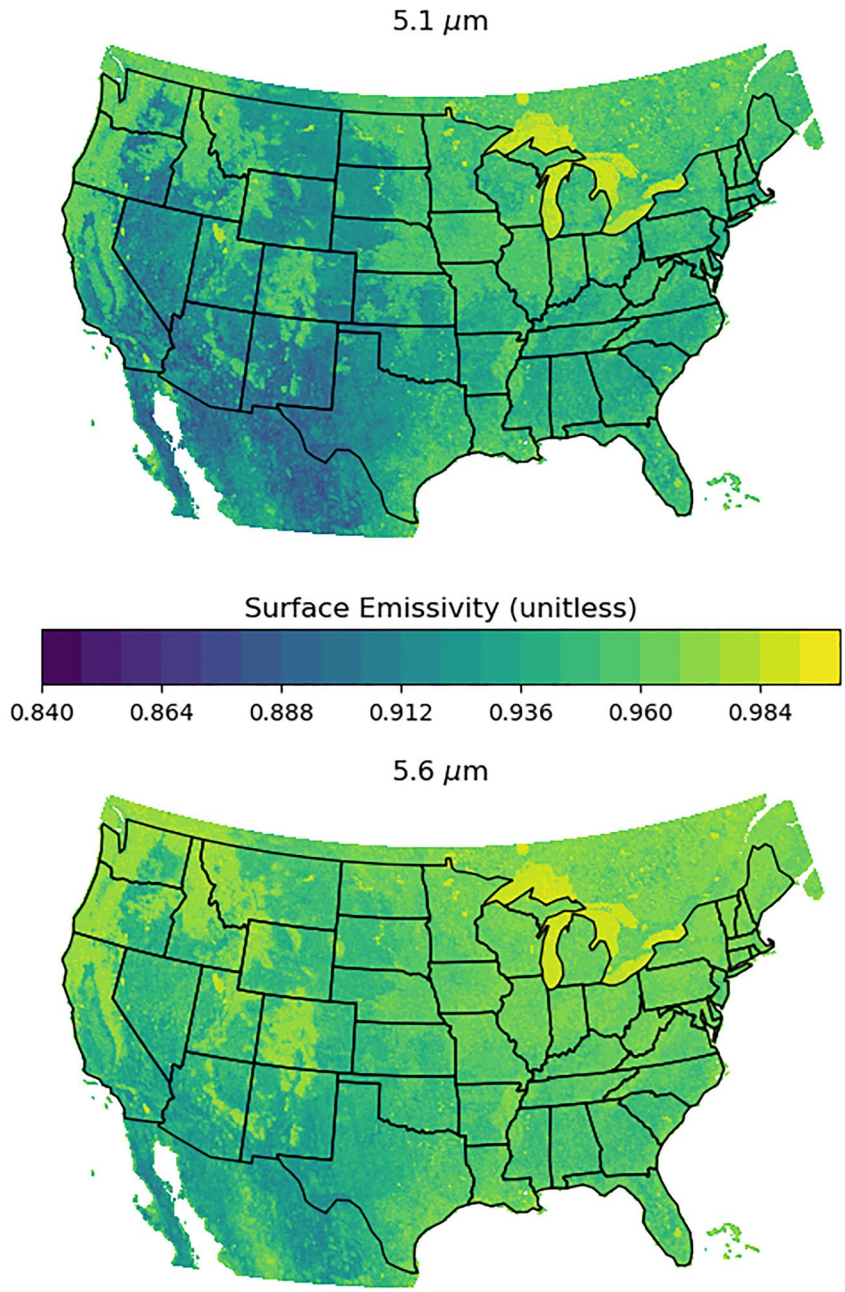

Figure 9. Surface emissivity at 5.1 μm (top) and 5.6 μm (bottom) on 1 June 2020. Values are derived from the Global Infrared Land Surface Emissivity Database (Seemann et al., 2008).

at 5.1 μm. The minimum emissivity at 5.1 μm(5.6 μm) is 0.840 (0.876), hence, for a perfectly transmissive atmosphere the maximum reflectance would be about 16%(12%) of the solar radiation at the TOA.

The two main factors that determine the atmospheric transmittance are the path length and amount of water vapor present throughout the column. Hence, we investigate how SZA and PWV modulate the reflected solar contribution to T_b under a range of surface emissivity conditions shown in Figure 9. The change in brightness temperature (ΔT_b) due to the reflected solar component is calculated by subtracting the T_b with sun below the horizon (SZA = 95) from the T_b with the sun above the horizon (SZA < 90). The range of PWV values shown in Figure 10 is manifested by scaling the water vapor profile of the U.S. Standard atmosphere by 10%–200% (1.3–26.0 mm). For PWV values greater than 25 mm the ΔT_b due to the reflected solar component at 5.1 μm becomes negligible

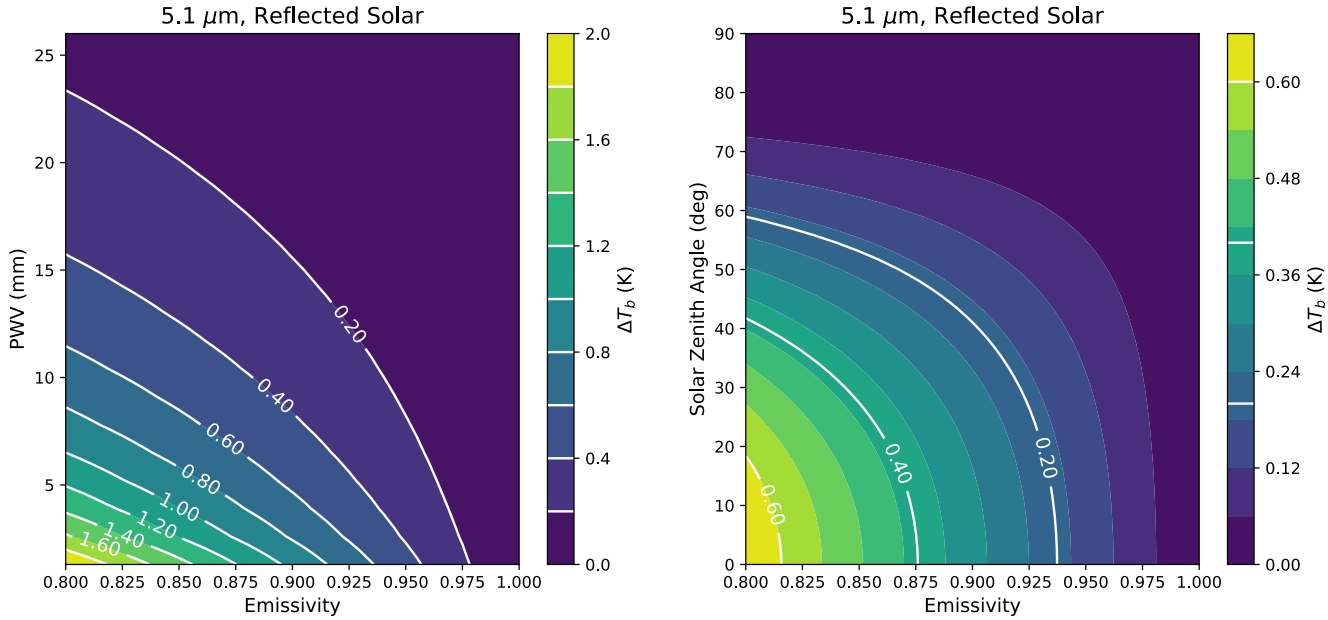

Figure 10. Reflected solar component at 5.1 μm. Left is the change in brightness temp due to precipitable water vapor (PWV) and emissivity with a SZA = 30°. PWV is scaled US std atm (0.1–2.0). Right is the change in brightness temp due to solar zenith angle and emissivity for the US std atm (PWV = 13 mm). Note the maximum range of each color bar are different, although the white contours are the same intervals.

and only is above 1 K for low surface emissivity (<0.9) and low moisture content (PWV < 7 mm). The right panel of Figure 10 shows how ΔT_b varies with changes in SZA and surface emissivity for the U.S. Standard atmosphere, indicating an even lower reflected solar component for larger SZAs. Overall, for a majority of conditions in the CONUS region the solar contribution will be small for the 5.1 μm band and even smaller for the 5.6 μm band (not shown). In fact, for the 5.6 μm band the largest ΔT_b for the variables shown in Figure 10 is 0.012 K for a surface emissivity of 0.8, SZA = 30, and scaled PWV of 10%, suggesting solar reflection will have no impact on the 5.6 μm band. Clouds will also reflect solar radiation but can be accounted for by using masking based on cloud detection from other standard geostationary imaging bands.

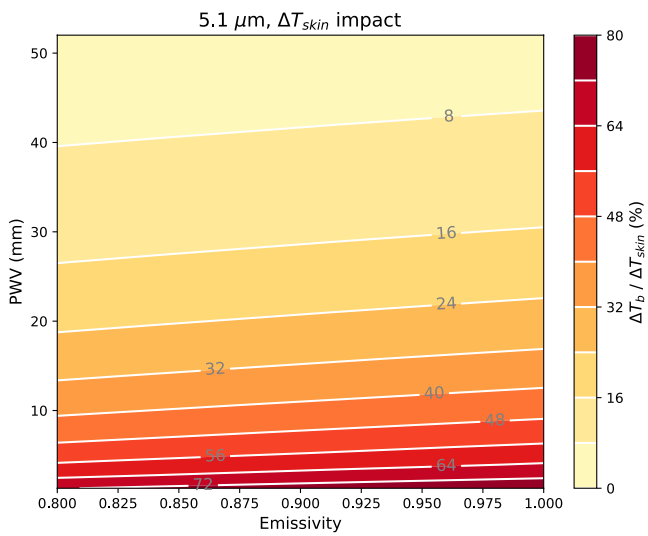

Figure 11. Impact of changes in the skin temperature on the observed brightness temperature ($\Delta T_b/\Delta T_{skin}$), at 5.1 μm, due to precipitable water vapor (PWV) and emissivity. PWV variability is accomplished by scaling the U.S. Standard Atmosphere (x0.1–4.0).

4.2. Surface Temperature

Water vapor imagery can be used for qualitative purposes as is currently done with ABI Band 10 at 7.3 μm. A complicating factor when using a band for qualitative analysis could be variable surface emission due to the diurnal cycle of the land surface temperature. If the atmosphere is transparent enough, changes in surface temperature will contribute to variations in brightness temperature. The weighting function of the 5.6 μm band (Figure 6) is essentially zero near the surface, whereas the weighting function of the 5.1 μm band (Figure 8) indicates a portion of observed radiance would originate from the surface for all six of the standard atmosphere cases.

The impact of changes in surface temperature on observed brightness temperatures is estimated by perturbing the modeled skin temperature (Figure 11). By increasing the skin temperature (T_{skin}) input into PCRTM by 1 K, the resulting change in the TOA radiance (ΔT_b) is computed. The ratio of the two values ($\Delta T_b/\Delta T_{skin}$) captures the relative change in radiance from surface temperature changes. Figure 11 shows this ratio expressed as a percentage for the 5.1 μm band. The contours show that this effect is non-negligible for the 5.1 μm band across a range of PWV values as $\Delta T_b/\Delta T_{skin}$ is greater than 24% for PWV values less than ~18–22 mm, with a small dependence on surface emissivity. Thus, the diurnal cycle of land temperatures will be an important

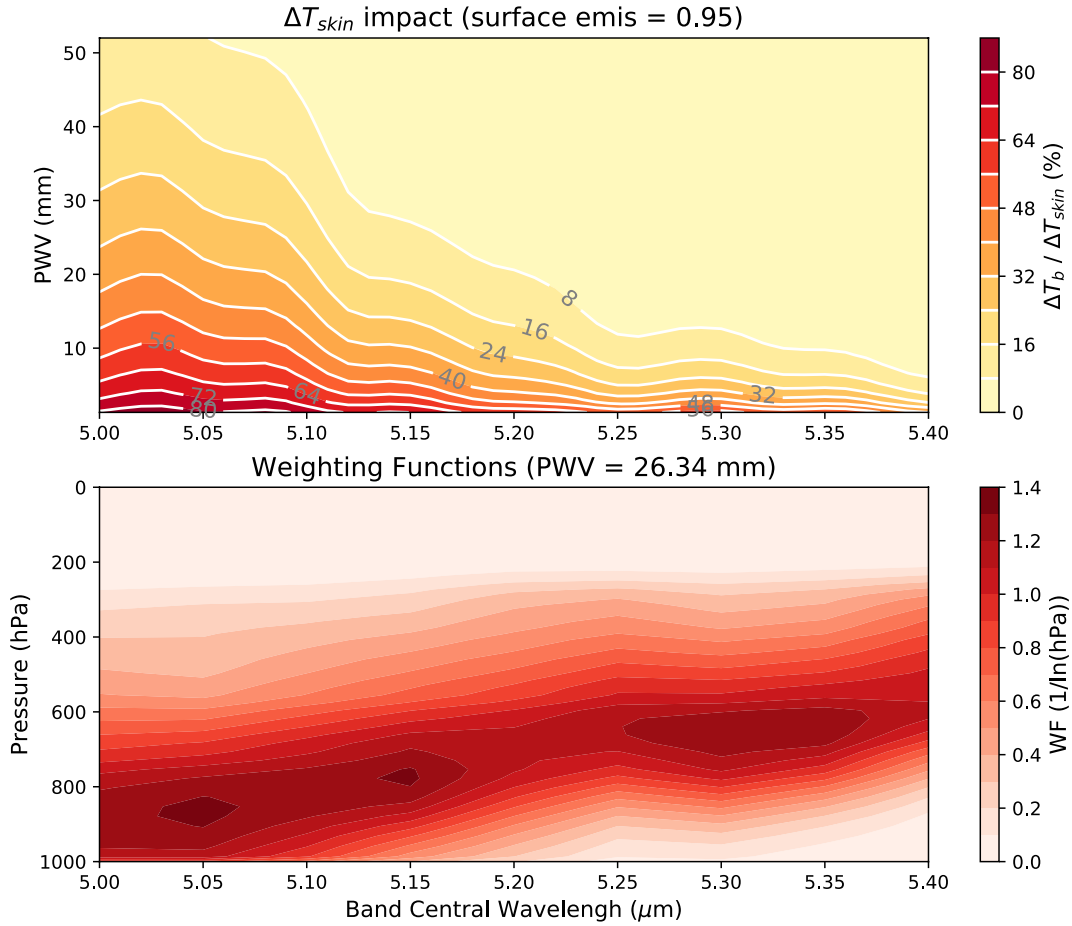

Figure 12. The surface impact, $\Delta T_b/\Delta T_{\text{skin}}$ (top panel) for precipitable water vapor (PWV) scaled values of the U.S. Standard Atmosphere (x0.1–4.0) and the weighting functions (bottom panel) for the mid-latitude standard atmosphere (PWV = 26.34 mm) for band central wavelengths ranging from 5.0 to 5.4 μm.

consideration when comparing day and night images. Keeping in mind likely complications due to the spectral dependence of the land surface emissivity, it is possible that the surface heating effect could be partially mitigated with complementary window channels sensitive to surface temperature.

For qualitative use of a low-level water vapor band, that may not utilize complementary channels, it is worth considering trade-offs in order to reduce surface temperature effects. By shifting the center wavelength to longer values it reduces the impact of the change in surface temperature on observed brightness temperatures because the weighting function is shifted to higher altitudes, hence limiting the overlap at the surface. The wavelength shift also increases the altitude at which water vapor is primarily detected. This trade-off is evident in Figure 12 which depicts how the surface temperature impact is most pronounced in drier conditions and for shorter wavelength bands (top panel). Concurrently, the weighting function is shifted to lower pressure levels for longer wavelength bands, when considering an atmospheric state with a given PWV, such as that of the mid-latitude summer atmosphere (bottom panel). The vertical resolution, as depicted by the weighting function, determines how close to the surface an instrument can detect water vapor before being affected by the radiation emitted at the surface. This trade-off is an important consideration for determining the final band characteristics.

5. Conclusions

New water vapor sensitive spectral bands are recommended for the next generation of imagers from geostationary orbit. Utilizing the short wavelength side of the water vapor absorption band offers a number of benefits, including improved spatial resolution due to less blurring from diffraction. In addition, there are fewer other absorbing

gases to interfere with the effect of water vapor absorption, simplifying the qualitative and quantitative analysis. Advances in low-level vapor vapor detection and finer spatial resolution in the mid-troposphere enhance our ability to predict weather events. Ultimately, the resultant imaging improvements will benefit society by strengthening forecast models and informing real-time decision making.

Two different methods find that a 5.6 μm band is comparable to that of the current ABI Band 10 at 6.95 μm in regards to the observed brightness temperatures and the mean pressure level at which the detected radiation was emitted from. The first method simulates brightness temperatures from a U.S. standard atmosphere, finding the smallest difference for a band centered at 5.595 μm. The second method compares weighting functions at 6.95 μm to that of a shifted band at 5.60 μm, resulting in a weighted mean pressure difference of only 3 hPa. These two methods find identical band centers at the accuracy possible from a practical standpoint. Continuity with past measurements is an important aspect of any future or follow-on mission so it is very encouraging to see imaging similarities using an IASI granule from METOP-A, convolved with both the 5.595 μm band and the current ABI Band 9. Furthermore, consistency in weighting function characteristics are beneficial in order to have similar vertical sensitivity to past measurements, while also opening the door to the possibility of improving observational capabilities.

A band centered at 5.1 μm is well suited to observe water vapor in the lower atmosphere, although this would not negate the need for hyper-spectral IR measurements from the geostationary orbit (Schmit et al., 2008). There are less absorbing gases on the short wavelength side compared to the long wavelength side of the water vapor absorption band allowing for a more straightforward interpretation of brightness temperature changes. The spatial distribution of observed brightness temperature is strongly influenced by the presence, or lack thereof, of moisture in the lower troposphere. This imaging capability is useful for detecting and tracking atmospheric rivers or cloud-free pre-convection over land. A unique band at 5.1 μm has a weighting function that peaks closer to the surface than what is currently available from geostationary orbit, providing the possibility of images of low-level water vapor as explored for a case on 7 December 2020. A future advanced geostationary imager would have the beneficial capability of enhanced spatial resolution compared to the IASI scenes shown in this paper, nonetheless it is clear that a 5.1 μm band would provide unique information not currently available from the existing 11.2 and 7.3 μm bands.

It is envisioned that a spectral band (centered near 5.1 μm) sensitive to boundary layer water vapor in conditionally unstable environments favorable for deep convection, is most likely to provide a benefit to operational meteorologists that produce short-term thunderstorm forecasts. The weighting functions of the three ABI water vapor bands (6.2, 6.9, and 7.3 μm) currently reveal limited if any insight into the character of boundary layer water vapor (below 800 hPa) for most mid-latitude and tropical atmospheres capable of supporting thunderstorms (Schmit et al., 2017). Though potentially challenging to use in quantitative products, brightness temperature contrasts due in part to differences in water vapor concentration associated with low-level jets transporting moisture can provide meteorologists situational awareness. This capability is especially valuable from the geostationary orbit due to the prospect of rapidly refreshing imagery where meteorologists could animate the 5.1 μm imagery. At sufficiently high spatial resolution, imagery may also evince atmospheric turbulence through gravity waves.

For atmospheric states with small amounts of water vapor in the atmospheric column there is an increased likelihood of the surface contributing to an observed brightness temperature change since there is little to no absorption by other gases. The reflected solar component is found to be less than 1 K except when considering PWV values below 7 mm and for low emissivity (relatively high reflectivity) surfaces. Also, changes in skin temperature affect observed brightness temperatures. For atmospheres with a PWV value less than about 20 mm, it is estimated that a given change in surface temperature will lead to more than a 24% change in the observed brightness temperature. Although land heating may be a factor for qualitative uses of the 5.1 μm band, it should be noted that very dry conditions are not the target application and there are strategies available to mitigate diurnal effects, such as utilizing infrared window bands that are primarily sensitive to surface emission. Ultimately, the center wavelength of a proposed low-level water vapor band could be shifted to longer wavelengths to reduce the surface emission contribution, but would detect water vapor higher in the atmosphere. The ideal central wavelength will depend on the approximate PWV for the meteorological applications where characterizing the pre-convective environment is important (i.e., moist atmospheres).

In order to implement these imaging capabilities from geostationary orbit there are various considerations that need to be investigated for optimal performance. Trade-offs must be considered between spectral band center wavelength and band width, signal-to-noise ratio, and optical capabilities. While the total radiance levels listed in Table 1 show the integrated radiance for the two proposed bands is smaller than ABI Bands 8–10, we note that real detectors fabricated for use at the shorter wavelengths may also have reduced noise levels. Many sensors (including the ABI) use HgCdTe photodetectors for these wavelength ranges, and we note that the internal noise is a strong function of the cutoff wavelength for the particular photodetector design (Rogalski, 2003). Furthermore, recent developments in infrared photodetectors design could lead to further reduced noise levels in the proposed wavelength ranges (Tan & Mohseni, 2018). While the engineering details of these promising bands at 5.1 and 5.6 μm are beyond the scope of this study, these detailed considerations are prime areas for future studies.

Data Availability Statement

The IASI datasets can be obtained from NOAA CLASS (https://www.avl.class.noaa.gov/release/glossary/IASI.htm) while the ABI Spectral Response functions can be found both on CIMSS (http://cimss.ssec.wisc.edu/goes/calibration/) and NOAA (https://ncc.nesdis.noaa.gov/GOESR/ABI.php) pages. The GOES ABI data was obtained through Amazon Web Services as part of the NOAA Big Data Program (https://registry.opendata.aws/noaa-goes/). The surface emissivity data can be obtained from the Global Infrared Land Surface Emissivity Database (http://cimss.ssec.wisc.edu/iremis/).

Acknowledgments
Drs. Daniel Lindsey and Andrew Heidinger are thanked for many probing questions related to this research. The views, opinions, and findings contained in this report are those of the authors and should not be construed as an official National Oceanic and Atmospheric Administration or U.S. government position, policy, or decision. This work was supported, in part, via NOAA Grants NA15NES4320001 and NA20NES4320003.

References

Ackerman, S. A., Platnick, S., Bhartia, P. K., Duncan, B., L'Ecuyer, T., Heidinger, A., et al. (2019). Satellites see the world's atmosphere. *Meteorological Monographs*, *59*, 4.1–4.53. https://doi.org/10.1175/amsmonographs-d-18-0009.1

Bessho, K., Date, K., Hayashi, M., Ikeda, A., Imai, T., Inoue, H., et al. (2016). An introduction to Himawari-8/9–Japan's new-generation geostationary meteorological satellites. *Journal of the Meteorological Society of Japan. Ser. II*, *94*(2), 151–183. https://doi.org/10.2151/jmsj.2016-009

Borbas, E. E., & Ruston, B. C. (2010). *The RTTOV UWiremis IR land surface emissivity module (Mission Report NWPSAF-MO-VS-042)*. EUMETSAT Satellite Application Facility on Numerical Weather Prediction. Retrieved from http://nwpsaf.eu/vs_reports/nwpsaf-mo-vs-042.pdf

Choi, Y.-S., & Ho, C.-H. (2015). Earth and environmental remote sensing community in South Korea: A review. *Remote Sensing Applications: Society and Environment*, *2*, 66–76. https://doi.org/10.1016/j.rsase.2015.11.003

Coddington, O., Lean, J. L., Pilewskie, P., Snow, M., & Lindholm, D. (2016). A solar irradiance climate data record. *Bulletin of the American Meteorological Society*, *97*(7), 1265–1282. https://doi.org/10.1175/bams-d-14-00265.1

Driemel, A., Augustine, J., Behrens, K., Colle, S., Cox, C., Cuevas-Agulló, E., et al. (2018). Baseline surface radiation network (BSRN): Structure and data description (1992–2017). *Earth System Science Data*, *10*(3), 1491–1501. https://doi.org/10.5194/essd-10-1491-2018

Gunshor, M. M., Schmit, T. J., Menzel, W. P., & Tobin, D. C. (2009). Intercalibration of broadband geostationary imagers using AIRS. *Journal of Atmospheric and Oceanic Technology*, *26*(4), 746–758. https://doi.org/10.1175/2008jtecha1155.1

Hannon, S. E., Strow, L. L., & McMillan, W. W. (1996). Atmospheric infrared fast transmittance models: A comparison of two approaches. In P. B. Hays, & J. Wang (Eds.), *Optical spectroscopic techniques and instrumentation for atmospheric and space research ii* (pp. 94–105). SPIE. https://doi.org/10.1117/12.256106

Hilton, F., Armante, R., August, T., Barnet, C., Bouchard, A., Camy-Peyret, C., et al. (2012). Hyperspectral Earth observation from IASI: Five years of accomplishments. *Bulletin of the American Meteorological Society*, *93*(3), 347–370. https://doi.org/10.1175/bams-d-11-00027.1

Holmlund, K., Grandell, J., Schmetz, J., Stuhlmann, R., Bojkov, B., Munro, R., et al. (2021). Meteosat Third Generation (MTG): Continuation and innovation of observations from geostationary orbit. *Bulletin of the American Meteorological Society*, *102*(5), E990–E1015. https://doi.org/10.1175/bams-d-19-0304.1

Liu, X., Smith, W. L., Zhou, D. K., & Larar, A. (2006). Principal component-based radiative transfer model for hyperspectral sensors: Theoretical concept. *Applied Optics*, *45*, 201–209. https://doi.org/10.1364/ao.45.000201

Liu, X., Yang, Q., Li, H., Jin, Z., Wu, W., Kizer, S., et al. (2016). Development of a fast and accurate PCRTM radiative transfer model in the solar spectral region. *Applied Optics*, *55*(29), 8236–8247. https://doi.org/10.1364/AO.55.008236

Matricardi, M., Chevallier, F., & Tjemkes, S. (2001). An improved general fast radiative transfer model for the assimilation of radiance observations. *Quarterly Journal of the Royal Meteorological Society*, *130*. https://doi.org/10.21957/1si9lq6pb

McClatchey, R. A., Fenn, R. W., Selby, J. E. A., Volz, F. E., & Garing, J. S. (1972). *Optical properties of the atmosphere (Rep. AFCRL-72-0497)*. Hanscom Air Force Base.

Menzel, W. P., Schmit, T. J., Zhang, P., & Li, J. (2018). Satellite-based atmospheric infrared sounder development and applications. *Bulletin of the American Meteorological Society*, *99*(3), 583–603. https://doi.org/10.1175/bams-d-16-0293.1

Minzner, R. A. (1977). The 1976 Standard Atmosphere and its relationship to earlier standards. *Reviews of Geophysics*, *15*(3), 375–384. https://doi.org/10.1029/RG015i003p00375

Morel, P., Desbois, M., & Szejwach, G. (1978). Correspondence. *Bulletin of the American Meteorological Society*, *59*(6), 711–714. https://doi.org/10.1175/1520-0477-59.6.711

Rogalski, A. (2003). Infrared detectors: Status and trends. *Progress in Quantum Electronics*, *27*(2), 59–210. https://doi.org/10.1016/s0079-6727(02)00024-1

Saunders, R., Matricardi, M., & Brunel, P. (1999). An improved fast radiative transfer model for assimilation of satellite radiance observations. *Quarterly Journal of the Royal Meteorological Society*, *125*, 1407–1425. https://doi.org/10.1002/qj.1999.49712555615

Schmit, T. J., Griffith, P., Gunshor, M. M., Daniels, J. M., Goodman, S. J., & Lebair, W. J. (2017). A closer look at the ABI on the GOES-R series. *Bulletin of the American Meteorological Society*, *98*(4), 681–698. https://doi.org/10.1175/bams-d-15-00230.1

Schmit, T. J., & Gunshor, M. M. (2020). *GOES-R Advanced Baseline Imager (ABI) algorithm theoretical basis document for Cloud and Moisture Imagery Product (CMIP) (Version 4)*. NOAA NESDIS, Center for Satellite Applications and Research.

Schmit, T. J., Gunshor, M. M., Menzel, W. P., Gurka, J. J., Li, J., & Bachmeier, A. S. (2005). Introducing the next-generation advanced baseline imager on GOES-R. *Bulletin of the American Meteorological Society*, *86*(8), 1079–1096. https://doi.org/10.1175/bams-86-8-1079

Schmit, T. J., Li, J., Ackerman, S. A., & Gurka, J. J. (2009). High-spectral- and high-temporal-resolution infrared measurements from geostationary orbit. *Journal of Atmospheric and Oceanic Technology*, *26*(11), 2273–2292. https://doi.org/10.1175/2009jtecha1248.1

Schmit, T. J., Li, J., Li, J., Feltz, W. F., Gurka, J. J., Goldberg, M. D., & Schrab, K. J. (2008). The GOES-R Advanced Baseline Imager and the continuation of current sounder products. *Journal of Applied Meteorology and Climatology*, *47*(10), 2696–2711. https://doi.org/10.1175/2008jamc1858.1

Schmit, T. J., Lindstrom, S. S., Gerth, J. J., Gunshor, M. M., & Gunshor, M. M. (2018). Applications of the 16 spectral bands on the advanced baseline imager (ABI). *Journal of Operational Meteorology*, *6*(4), 33–46. https://doi.org/10.15191/nwajom.2018.0604

Seemann, S. W., Borbas, E. E., Knuteson, R. O., Stephenson, G. R., & Huang, H.-L. (2008). Development of a global infrared land surface emissivity database for application to clear sky sounding retrievals from multispectral satellite radiance measurements. *Journal of Applied Meteorology and Climatology*, *47*(1), 108–123. https://doi.org/10.1175/2007jamc1590.1

Smith, S. , W. L., Revercomb, H., Bingham, G., Larar, A., Huang, H., Zhou, D., et al. (2009). Technical note: Evolution, current capabilities, and future advance in satellite nadir viewing ultra-spectral ir sounding of the lower atmosphere. *Atmospheric Chemistry and Physics*, *9*(15), 5563–5574. https://doi.org/10.5194/acp-9-5563-2009

Tan, C. L., & Mohseni, H. (2018). Emerging technologies for high performance infrared detectors. *Nanophotonics*, *7*(1), 169–197. https://doi.org/10.1515/nanoph-2017-0061

Wu, X., Hewison, T., & Tahara, Y. (2009). GSICS GEO-LEO intercalibration: Baseline algorithm and early results. *Proceedings of SPIE - The International Society for Optical Engineering*, 7456. https://doi.org/10.1117/12.825460

Yang, J., Zhang, Z., Wei, C., Lu, F., & Guo, Q. (2017). Introducing the new generation of Chinese geostationary weather satellites, Fengyun-4. *Bulletin of the American Meteorological Society*, *98*(8), 1637–1658. https://doi.org/10.1175/bams-d-16-0065.1